Bull. Mater. Sci. (2021)44:225
https://doi.org/10.1007/s12034-021-02506-2

Influence of Cd content on structural and optical properties of chemical bath deposited $Cd_xPb_{1-x}S$ thin films

LIPIKA GOGOI[1,*], S CHALIHA[2], DIBYA JYOTI BORAH[3] and P K SAIKIA[1]

[1]Thin Film Laboratory, Department of Physics, Dibrugarh University, Dibrugarh 786004, India
[2]Thin Film and Device Research Laboratory, Department of Physics, Bahona College, Jorhat 785101, India
[3]Material Science Laboratory, Department of Physics, Dibrugarh University, Dibrugarh 786004, India
*Author for correspondence (lipikagogoi5@gmail.com)

MS received 9 March 2021; accepted 28 April 2021

Abstract. This paper describes the preparation and characterization of nanocrystalline $Cd_xPb_{1-x}S$ thin films by chemical bath deposition method with different Pb and Cd solute ratios. XRD, HRTEM and SAED patterns show the nanocrystalline nature of films with the co-existence of cubic, hexagonal and tetragonal phases, while micro-Raman spectra reveals the presence of cubic and hexagonal phases in the films. The average crystallite size of $Cd_xPb_{1-x}S$ estimated from TEM and XRD methods were nearly same. The chemical bonding present in the films was studied by FTIR spectral analysis. SEM images show uniformly distributed grains of different sizes over the substrates. Optical studies show the prominent blue shift in band gap energy (E_g) with the increase in Cd content in PbS. The increment of Cd addition to $Cd_xPb_{1-x}S$ has led to enhance the transmittance as well as band gap energy.

Keywords. $Cd_xPb_{1-x}S$; CBD; XRD; Raman spectra; HRTEM; SAED; band gap.

1. Introduction

The metal chalcogenide-based binary and ternary compound semiconductors are of great interest because of their relatively easy fabrication process and having their potential applications in electronic and optoelectronic devices [1]. By alloying appropriate binary constituents with changes in their relative concentrations, ternary alloys provide a class of semiconductors in which lattice parameters, band gap energy and other parameters could be continuously varied within specific limits [2]. The II–IV–VI group ternary semiconductor inorganic compounds, in thin-film form, have attracted great attention due to their unique physical properties and wide range of applications [3,4]. Lead sulphide (PbS) is a IV–VI group semiconductor with a narrow band gap of ~0.41 eV [5]. The narrow band gap of PbS could be used for certain photovoltaic devices with high sensitivity to the infrared (IR) spectral domain [6]. PbS has large Bohr radius of ~18 nm [7]. These properties of PbS provide strong quantum confinement of holes and electrons in nano-sized structure, so that the value of optical band gap can be controlled by modifying the crystallite size, according to the effective mass model [8,9]. By altering the material's dimensionality, it is also possible to control electrical as well as optical properties [10]. PbS has been used in various devices viz. diode lasers, IR detectors, sensors, transistors, contact rectifiers and solar cells [11].

Cadmium sulphide (CdS) with direct band gap of ~2.46 eV and Bohr radius of ~2.5 nm, is a kind of II–VI group semiconductor material which has attracted much attention because of its application in various optoelectronic devices viz. solar cells, photo detectors, thin film transistors and light emitting diodes [12–14]. Owing to high electrochemical stability, high carrier concentration and high absorption coefficient, CdS is used as an optimize window layer for CdTe and other chalcopyrite-based solar cells [15–17]. Therefore, mixed nanostructures based on PbS and CdS, i.e., $Cd_xPb_{1-x}S$ has dealt with immense interest of research. Because, it offers the advantage of tuning the optical and optoelectronic properties of both CdS and PbS, viz. band gap, electrical conductivity and thermoelectric power in a controlled manner [18]. One of the most characteristic advantages of $Cd_xPb_{1-x}S$ semiconductor compound is high irradiation stability, which makes it useful for radiation hazardous facilities [19]. Tuneable composition of $Cd_xPb_{1-x}S$ provides a wide range of variations in optical band gap, and it is possible to widen the spectral window [20]. $Cd_xPb_{1-x}S$ ternary thin films have been chosen to enhance the solar energy conversion from ultraviolet (UV) to near infrared (NIR) spectral region [21]. There are various deposition techniques for the preparation of CdS and PbS thin films. Currently, the most used deposition methods to prepare ternary films are chemical bath deposition (CBD) [22–25], electro deposition [26–29], flash evaporation

Published online: 07 August 2021

[30–32], spray pyrolysis [33,34], successive ionic layer adsorption and reaction (SILAR) [35,36], magnetron sputtering [37,38]. Among them, CBD is one of the simplest and highly efficient method. It has simple routine, low-cost, homogeneity and reproducibility [39,40].

The most recognized manifestation of nanocrystalline thin films is tunability of band gap with increase and decrease in crystal size. The narrow band gap of PbS (0.41 eV) semiconductor can be modified by adding different solute ratios of a wide band gap of CdS (2.4 eV). Nair *et al* [1] have investigated the effect of Cd/Pb atomic% on the structural, optical and electrical properties of CdPbS films by changing the molarity of the precursors used for the preparation of the films by CBD technique. Tan *et al* [2] have synthesized ternary $Cd_xPb_{1-x}S$ nanocrystal with clean surface and homogeneous composition by mechanical alloying process [2]. Deo *et al* [3] have prepared $Cd_{0.5}Pb_{0.5}S$ thin films by CBD method to investigate the structural, morphological and optical characteristics as a function of temperature. Barote *et al* [4] have fabricated $Cd_{1-x}Pb_xS$ thin films by CBD method at various optimum parameters to study the growth mechanics and reduction kinetics. Many of the previous research articles of $Cd_{1-x}Pb_xS$ composition and their thin films were not exposed to the discussion of the influence of cadmium concentration on the structural and composition of $Cd_xPb_{1-x}S$ thin films. Therefore, the motivation of the present work is to study the influence of cadmium content on the structural, morphological and optical properties of $Cd_xPb_{1-x}S$ thin films. In the present work, $Cd_xPb_{1-x}S$ thin films are grown by cost-effective CBD technique at different solute ratios of (Pb:Cd) and also, to study the applicability of the prepared $Cd_xPb_{1-x}S$ thin films for photovoltaic device applications.

2. Experimental

$Cd_xPb_{1-x}S$ thin films were deposited onto chemically cleaned glass substrates at deposition temperature of 60°C for 120 min by using CBD technique. First, 3 ml of 0.1 M lead acetate ($Pb(CH_3COO)_2{\cdot}2H_2O$) was taken as Pb^{2+} ion source. To this, 0.1 M cadmium acetate ($Cd(CH_3COO)_2{\cdot}2H_2O$) solution with different volume (7, 12, 17 and 22 ml) was used as Cd^{2+} ion source. A 10 ml of 0.5 M thiourea (CH_4N_2S) was used as S^{2+} ion source for all the samples in the bath solution for the deposition of $Cd_xPb_{1-x}S$ thin films. The pH of the solution was maintained at 12.4 by adding liquid NH_3 and triethanolamine (TEA) was used as a complexing agent. Deionized water was used as a solvent throughout the process. The prepared films are golden yellow in colour. In this work, four samples were prepared by changing the solute ratio of Pb and Cd (Pb:Cd) as 3:7, 3:12, 3:17 and 3:22. The samples are coded as S_1, S_2, S_3 and S_4, respectively. The sample details of the $Cd_xPb_{1-x}S$ thin films prepared by CBD method are listed in table 1.

X-ray diffractometer (XRD), model: X'Pert Pro, Phillips, using CuKα radiation (λ = 1.5406 Å) as a source is used to determine the crystal structure of the deposited powder sample. Fourier transform of infrared (FTIR), model: IMPACT410, spectra were taken on spectrometer with software OMNIC E.S.P.5.0, to investigate the chemical bonding structure of the $Cd_xPb_{1-x}S$ thin films. Raman spectroscopy (Renishaw basis series with 514 Laser) is used to perform micro-Raman studies. Surface morphology and the chemical composition of the prepared films were obtained by scanning electron microscope (SEM), model: JEOL JSM IT-300, equipped with energy-dispersive X-ray (EDX) spectroscopy attachment. High resolution transmission electron microscopy (HRTEM) and selected area electron diffraction (SAED) pattern were done by transmission electron microscope (TEM), model: JEM-2100, JEOL, operated with an acceleration voltage of electron beam ~200 kV. The thickness of the prepared films was estimated by Tolansky method using green line (λ = 5461 Å) of mercury. For optical studies, absorption and transmission spectra were recorded by UV–Vis spectrophotometer, model: Shimadzu UV–Vis 1800, in the wavelength range of 200–1100 nm.

3. Results and discussion

3.1 *XRD analysis of $Cd_xPb_{1-x}S$ thin films*

Figure 1 shows the XRD patterns of samples S_1, S_2, S_3 and S_4. A comparison of the peak position (2θ) values of XRD spectra with JCPDS data shows that the films have mixed phase structures of cubic, hexagonal and tetragonal, exhibiting the nanocrystalline nature. The peaks at 2θ of 20.65, 34.77 and 41.61° can be indexed to the planes (110), (211) and (113), respectively, of tetragonal PbS (JCPDS card no. 20-0596). The peaks at 24.80, 26.50, 43.68, 47.83, 51.82 and 58.27° match with the planes (100), (002), (110), (103), (112) and (202), respectively, which can be indexed to hexagonal CdS (JCPDS card no. 41-1049). The diffraction peaks at 53.45 and 71.03°, which match the planes (222) and (420), respectively, are indexed to cubic PbS (JCPDS card no. 05-0592). The intensities and the number of the peaks decrease considerably with the increase in Cd contents in $Cd_xPb_{1-x}S$ films. This is attributed to the increase in disorder with the incorporation of Cd at Pb sites in PbS [41]. A decrease in lattice spacing d for all the $Cd_xPb_{1-x}S$ films has been occurred. Due to the smaller ionic radii of Cd^{2+} (0.91 Å) [42] than Pb^{2+} (1.21 Å) [43], the lattice would undergo contraction as Cd^{2+} occupies the Pb^{2+} sites in the host lattice. Similar works have been reported for CdPbS thin films and other ternary systems by other researchers [44–47]. There is an increase in heterogeneity of the films for the occupation of Cd into the host lattice PbS. As a result, the peak broadening occurs in the films and also, the particle size decreases [48,49]. The

Table 1. Sample details of all the prepared $Cd_xPb_{1-x}S$ thin films.

Sl. no.	Sample code	Molarity	Solute ratios in ml (Pb:Cd)	Thiourea in ml (S)
1	S_1	0.1 M	3:7	10
2	S_2		3:12	10
3	S_3		3:17	10
4	S_4		3:22	10

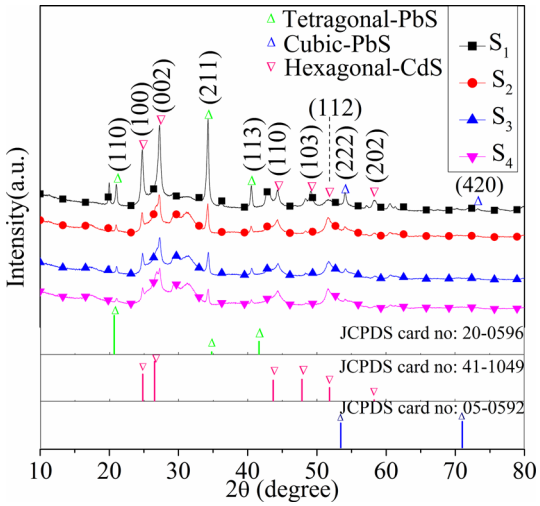

Figure 1. XRD spectra of $Cd_xPb_{1-x}S$ thin film samples S_1, S_2, S_3 and S_4. Green, pink and blue patterns represent standard phases of tetragonal-PbS, hexagonal-CdS and cubic-PbS peaks, respectively.

stable crystal structures of PbS and CdS are different. Therefore, the crystal structure of $Cd_xPb_{1-x}S$ becomes unstable when Cd^{2+} occupies more sites of Pb^{2+} in the host lattice [50]. To stabilize the $Cd_xPb_{1-x}S$ crystal structure, the crystallite size is reduced to release the strain [51].

3.2 *Crystallite size and strain*

3.2a *Scherrer's method:* The average crystallite size (D) of the films is estimated by using Scherrer's equation (1) [52]:

$$D = \frac{K\lambda}{\beta \cos\theta} \tag{1}$$

where K is a constant equal to 0.99, β the full width at half maxima (FWHM) and θ the Bragg's diffraction angle. The average crystallite sizes of samples S_1, S_2, S_3 and S_4 are found to be ~24, 20, 15 and 12 nm, respectively. The crystallite size decreases with the increase in Cd content in $Cd_xPb_{1-x}S$ thin films, and are shown in table 2.

3.2b *Williamson–Hall method:* Owing to the crystal imperfections and distortions, the strain (ε) induced-broadening of XRD peak arises and is related by $\varepsilon \approx \beta_s/\tan\theta$ [53]. Williamson–Hall (W–H) method like Scherrer's equation does not obey $1/\cos\theta$ dependency, but varies with $\tan\theta$. A simple integral breadth method is used in W–H method by considering the peak broadening as a function of 2θ, where both size- and strain-induced XRD peak broadenings are deconvoluted [54]. Addition of Scherrer's equation and $\varepsilon \approx \beta_s/\tan\theta$, Williamson–Hall (W–H) suggested for broadened peaks as [53]:

$$\beta_T \cos\theta = 4\varepsilon \sin\theta + \frac{k\lambda}{D} \tag{2}$$

Equation (2) represents the uniform deformation model (UDM), where the strain was assumed to be uniform in all the crystallographic directions. For a multiple-ordered diffraction pattern of a film, for each peak, found at different 2θ, β values are different. W–H plots for all samples S_1, S_2, S_3 and S_4 are shown in figure 2a–d. The average values of crystallite size (D) and strain (ε) are estimated from intercept and slope of the linear fitted W–H plot, respectively. The values of D and ε of the different films are summarized in table 2. The average value of crystallite size is found to decrease with the increase in Cd content in $Cd_xPb_{1-x}S$, while strain is increased.

3.2c *Size–strain plot method:* W–H plots showed isotropic line broadening. However, a better evaluation of the size–strain parameters can be obtained in case of isotropic line broadening by considering an average size–strain plot (SSP) [53,55]. Accordingly, one can obtain [53]:

$$(d_{hkl}\beta_{hkl}\cos\theta)^2 = K/D\left(d_{hkl}^2\beta_{hkl}\cos\theta\right) + (\varepsilon/2)^2. \tag{3}$$

In SSP plot, $(d_{hkl}\beta_{hkl}\cos\theta)^2$ is plotted with respect to $(d_{hkl}^2\beta_{hkl}\cos\theta)$ for all the orientated peaks of $Cd_xPb_{1-x}S$ thin films. SSP plot for samples S_1, S_2, S_3 and S_4 are shown in figure 3a–d. The values of the crystallite size and the strain are determined from the slope and the square root of the y-axis intercept of linearly fit data. The obtained values are listed in table 2. From these plots, it is observed that with the increase in Cd content, the average crystallite size decreases and average strain increases. The variation in the estimation of crystallite size by Scherrer's, W–H and SSP methods is due to different average particle size distribution [56].

Table 2. Estimated average crystallite size and average strain of the $Cd_xPb_{1-x}S$ thin films.

Sample code	Scherrer's method	W–H analysis (UDM)		SSP method	
	Crystallite size, D (nm)	Crystallite size, D (nm)	Strain $\varepsilon \times 10^{-3}$	Crystallite size, D (nm)	Strain $\varepsilon \times 10^{-3}$
S_1	24	39	2.01	20	6.87
S_2	20	33	6.53	18	11.29
S_3	15	24	8.03	11	17.91
S_4	12	21	9.40	7	25

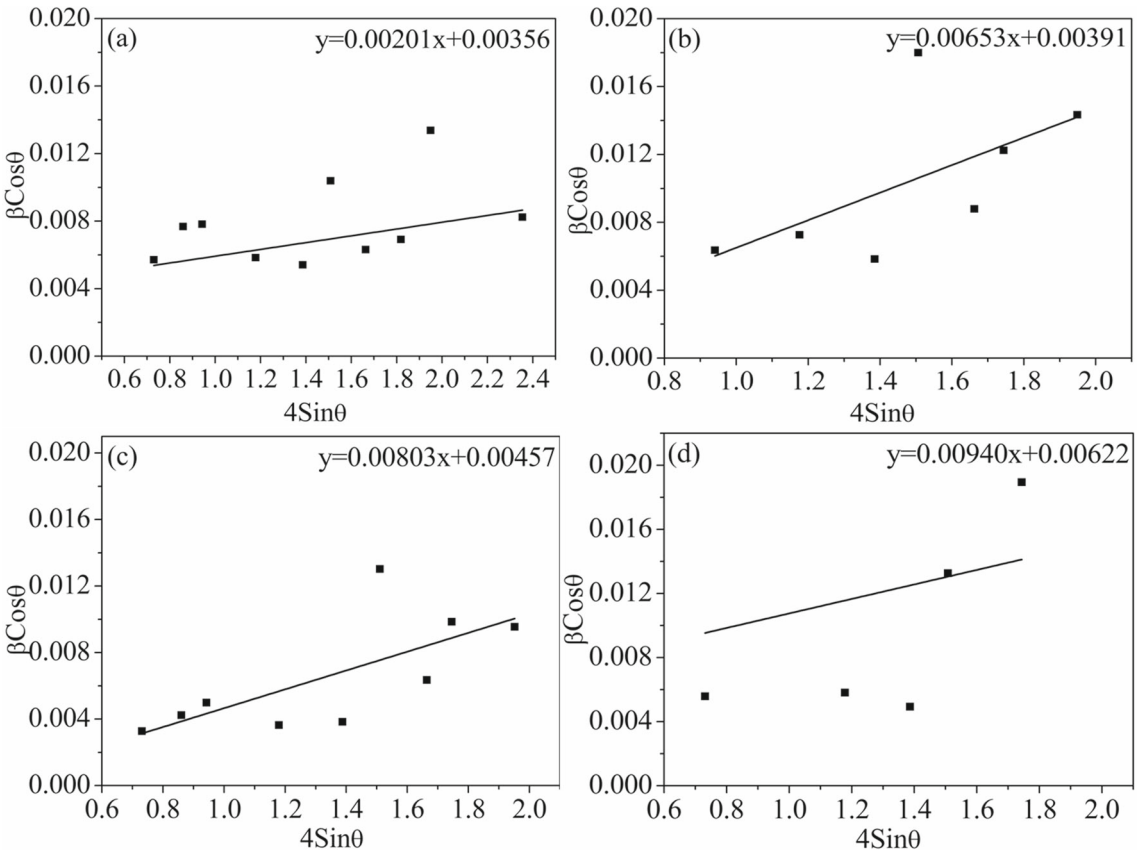

Figure 2. W–H plots of $Cd_xPb_{1-x}S$ thin film samples prepared at different solute ratios of (Pb:Cd) assuming UDM: (**a**) S_1 (3:7), (**b**) S_2 (3:12), (**c**) S_3 (3:17) and (**d**) S_4 (3:22), respectively.

3.3 *FTIR characteristics of $Cd_xPb_{1-x}S$ thin films*

To study the molecular arrangements present in the sample, FTIR spectra of samples S_1, S_2, S_3 and S_4 are recorded in the wavenumber range of 1100–400 cm^{-1}, as shown in figure 4. The frequency bands at ~1032 and 1074 cm^{-1} correspond to the C–O stretching vibration due to acetate group present in the sample [57–59]. The peaks at ~850 and 900 cm^{-1} are assigned to C–S bond due to sulphide group present in thiourea for all the samples [60,61]. In addition, other strong characteristics for Cd–S stretching vibrations occurred at ~651 and 680 cm^{-1} [62–64]. The characteristic absorption peaks for weak Pb–S vibrational bond of all the samples are identified at ~419 cm^{-1} [7].

3.4 *Micro-Raman characteristics of $Cd_xPb_{1-x}S$ thin films*

In case of wurtzite CdS, there are six observable Raman active modes, E_2 at 43 cm^{-1}, A_1 transverse optical, A_1(TO) at 234 cm^{-1}, E_2 at 256 cm^{-1}, E_1(TO) at 243 cm^{-1}, A_1 longitudinal optical, A_1(LO) at 305 cm^{-1} and E_1(LO) at

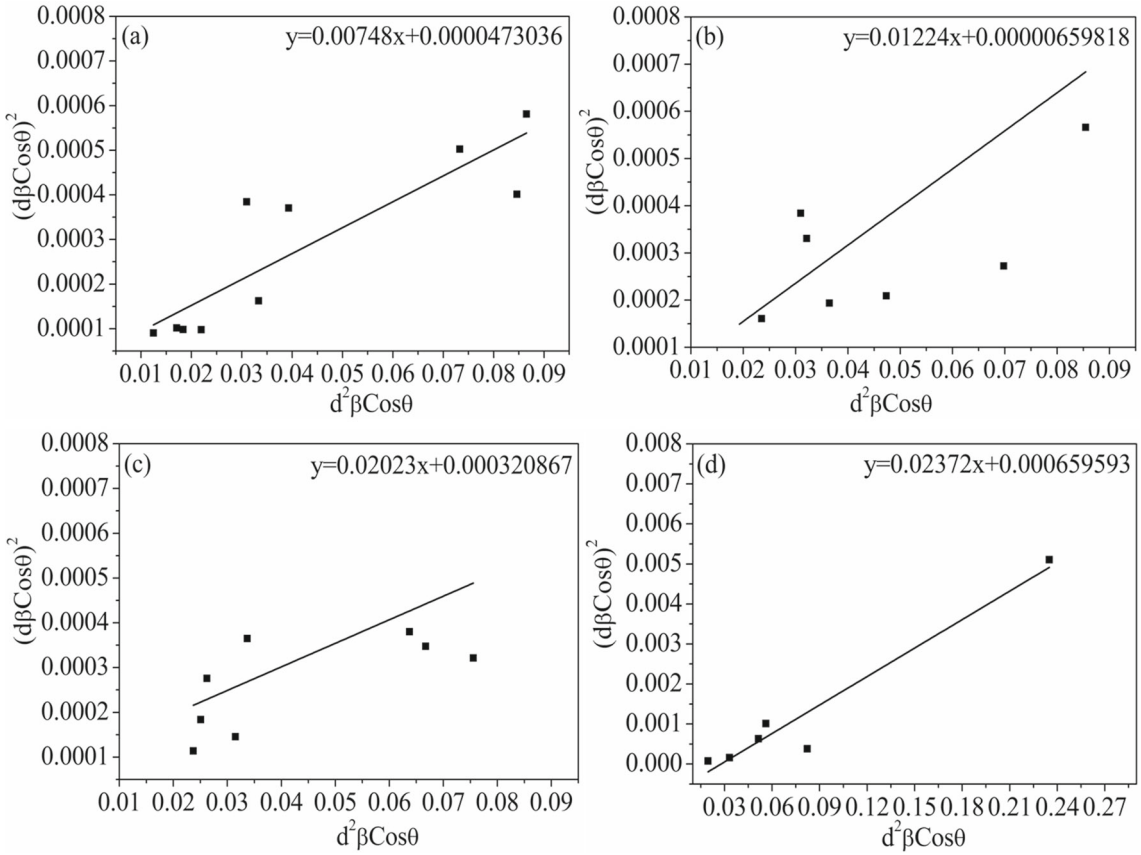

Figure 3. SSP plots of $Cd_xPb_{1-x}S$ thin film samples prepared at different solute ratios of (Pb:Cd): (**a**) S_1 (3:7), (**b**) S_2 (3:12), (**c**) S_3 (3:17) and (**d**) S_4 (3:22), respectively.

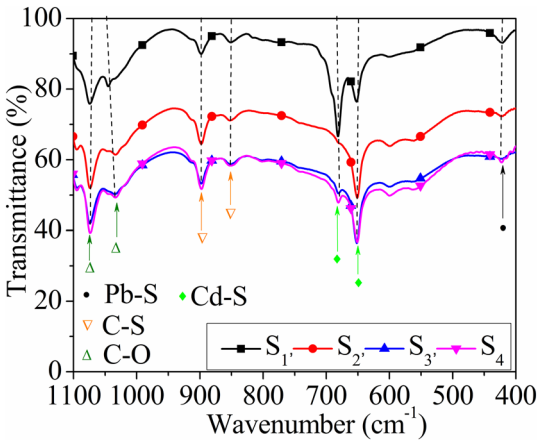

Figure 4. FTIR spectra of $Cd_xPb_{1-x}S$ thin film samples prepared at different ratios of (Pb:Cd): S_1 (3:7), S_2 (3:12), S_3 (3:17) and S_4 (3:22).

307 cm^{-1} [65]. TO and LO modes of cubic modification coincide with E_1(TO) and E_1(LO) of the hexagonal modification. Figure 5a–d shows the Raman spectra of all samples S_1, S_2, S_3 and S_4, respectively. The prominent Raman peaks of samples S_1, S_2, S_3 and S_4 are at ∼303, 302.3, 302.4 and 302 cm^{-1}, respectively. These peaks are attributed to either cubic 1LO phonon or hexagonal A_1(LO)/E_1(LO) phonons, whereas 2 and 3 cm^{-1} are the respective shifts from 305 cm^{-1} of the single crystal CdS [66]. All the films have least shifts indicating that the films have better crystal structure [67]. Another characteristic peak, 2LO phonon is barely noticeable at about ∼612.5–610.1 cm^{-1}. Also, in the spectrum, some tiny peaks are observed. The peaks observed at ∼266.7 (S_1), 268.4 (S_2), 267.4 (S_3) and 266.7 cm^{-1} (S_4) are the E_2 peaks of hexagonal CdS [68–70]. However, the peaks observed at ∼276–287 cm^{-1} are attributed to either the TO peak of cubic CdS or E_1(TO) peak of hexagonal CdS [65,71,72]. Both the cubic and hexagonal phases of CdS are observed in the samples. All the observed Raman peaks are listed in table 3.

A Gaussian fit is applied to the 1LO peak observed at ∼302–303 cm^{-1} for all samples S_1, S_2, S_3 and S_4 are shown in figure 6a–d, respectively. The observed peaks have FWHM of ∼21.7, 22, 24.5 and 27.8 cm^{-1} for S_1, S_2, S_3 and S_4, respectively. It shows that FWHM of the prepared samples increases with the increasing Cd content in $Cd_xPb_{1-x}S$ films and indicates a diminution in film crystallinity [66,67]. This result is consistent with the XRD results.

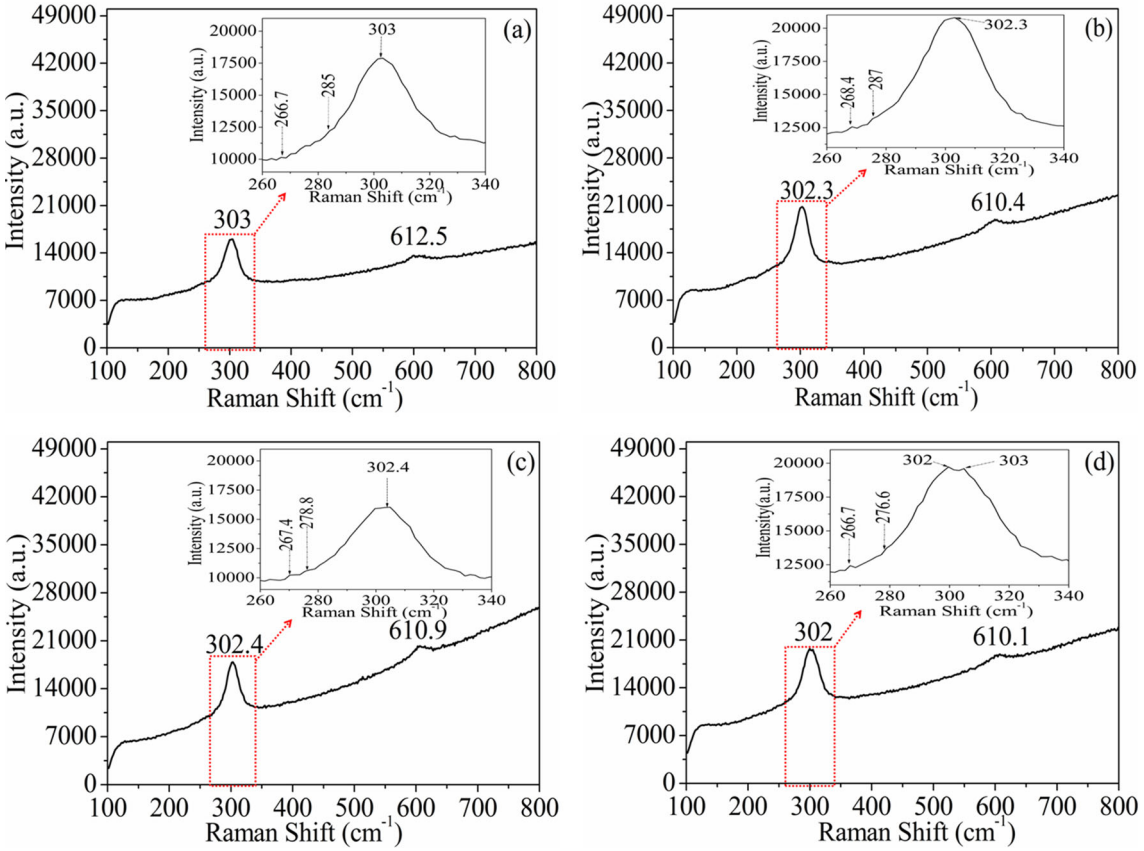

Figure 5. Micro-Raman spectra of $Cd_xPb_{1-x}S$ thin film samples prepared at different ratios of (Pb:Cd): (**a**) S_1 (3:7), (**b**) S_2 (3:12), (**c**) S_3 (3:17) and (**d**) S_4 (3:22), respectively. Inset shows the magnified area of the micro-Raman spectra in Raman shift range of 260–340 cm^{-1} corresponding to the samples.

Table 3. Estimated peak position, FWHM and phase assignment from micro-Raman characteristics.

Sample code	Hexagonal phase					Cubic phase			FWHM (cm^{-1})
	E_1(LO)	A_1(LO)	E_1(TO)	A_1(TO)	E_2	1LO	TO	2LO	
S_1	303	303	285	—	266.7	303	285	612.5	21.7
S_2	302.3	302.3	287	—	268.4	302.3	287	610.4	22
S_3	302.4	302.4	278.8	—	267.4	302.4	278.8	610.9	24.5
S_4	302 303	302 303	276.4	—	266.7	302 303	276.4	610.1	27.8

3.5 *Surface morphology and compositional analysis of $Cd_xPb_{1-x}S$ thin films*

The surface morphology of all the $Cd_xPb_{1-x}S$ thin films deposited at different solute ratios (Pb:Cd) with the magnification of ×5000 is shown in figure 7. The morphology of the samples represents layered type structure in samples S_1 and S_2, as shown in figure 7a, b, respectively. By increasing the Cd content in $Cd_xPb_{1-x}S$, more cabbage like structures are observed in samples S_3 and S_4, which are shown in figure 7c, d, respectively. In each sample, the surface is composed of largely compact interconnected grains with different sizes and sharp edges. Grains are uniformly distributed over the glass substrates without any visible microscopic defects, like cracks or pinholes. The average grain sizes of samples S_1, S_2, S_3 and S_4 are determined by Image J software and found to be ∼92, 86, 72 and 63 nm, respectively. It is observed that the grain size of the samples decreases with the increase in Cd content in the deposited films. This confirms that the disordering increases with the increase in Cd incorporation in host lattice and results in a small grain growth [44]. This result is

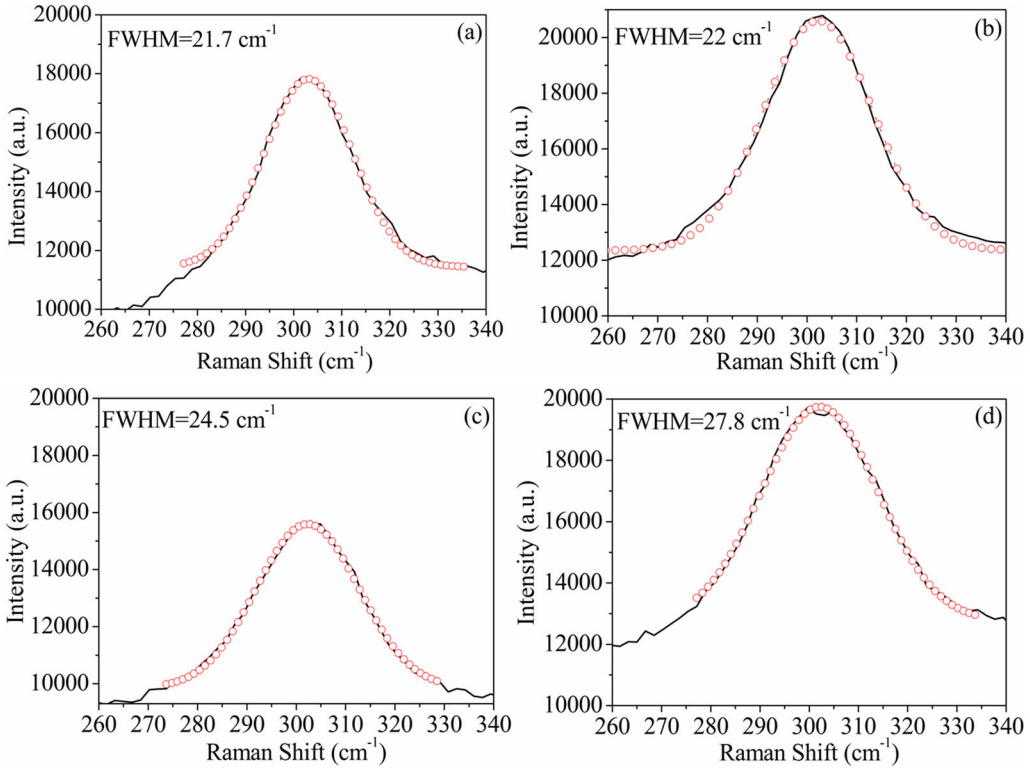

Figure 6. Deconvolution of cubic 1LO or hexagonal $A_1(LO)/E_1(LO)$ peak of Raman spectra for the samples: (**a**) S_1, (**b**) S_2, (**c**) S_3 and (**d**) S_4, respectively.

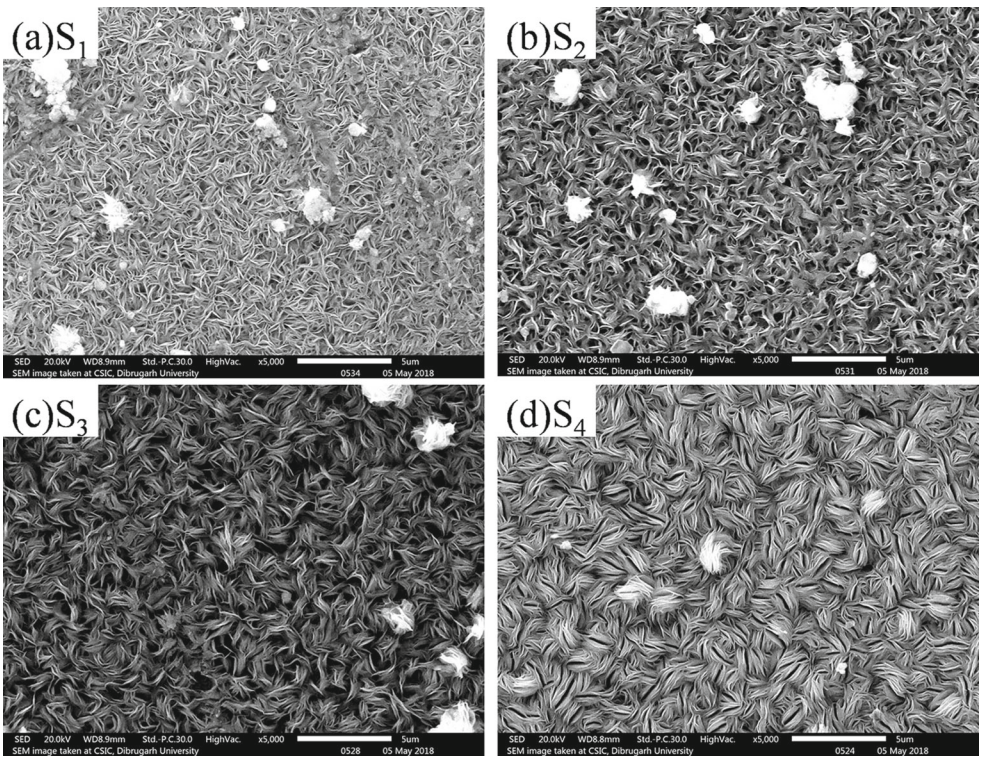

Figure 7. SEM images of $Cd_xPb_{1-x}S$ thin films prepared at different solute ratios of (Pb:Cd): (**a**) S_1 (3:7), (**b**) S_2 (3:12), (**c**) S_3 (3:17) and (**d**) S_4 (3:22), respectively.

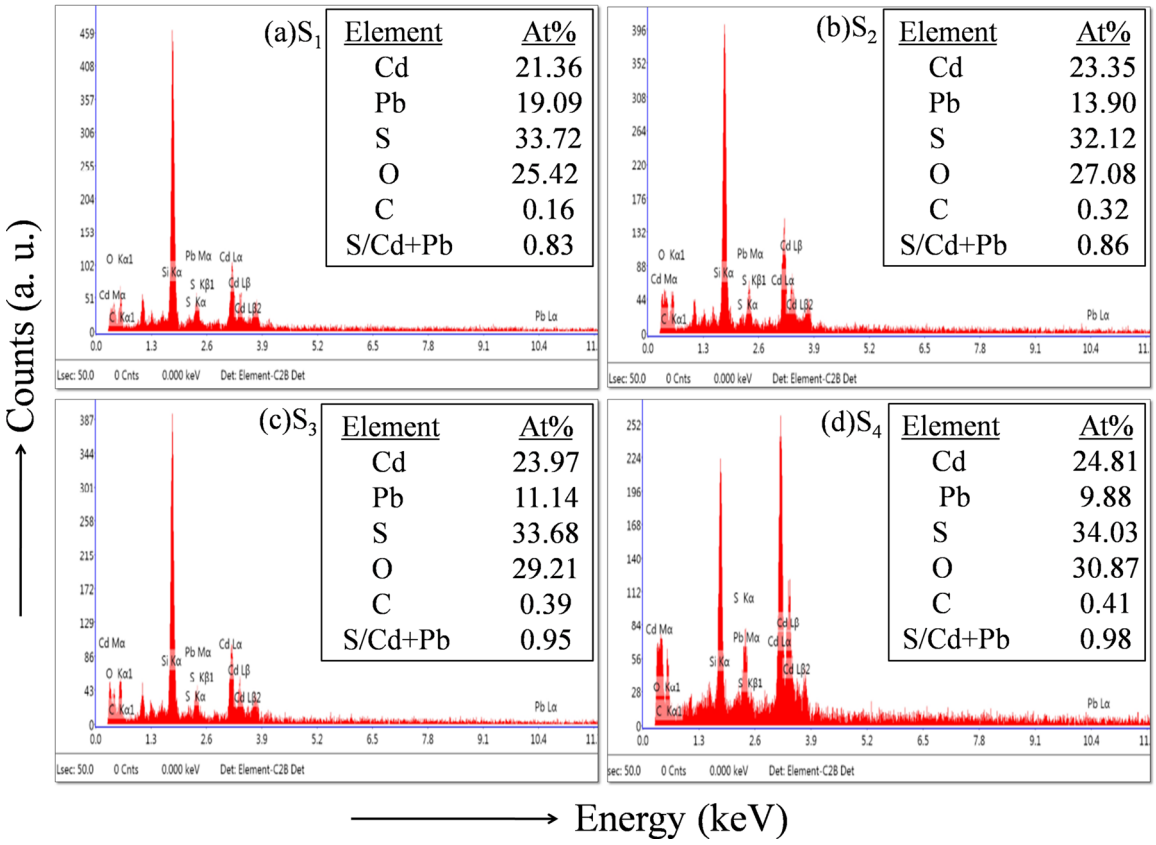

Figure 8. EDX spectra of $Cd_xPb_{1-x}S$ thin film samples: (**a**) S_1, (**b**) S_2, (**c**) S_3 and (**d**) S_4, respectively. Inset shows the atomic% ratios of S/(Cd+Pb).

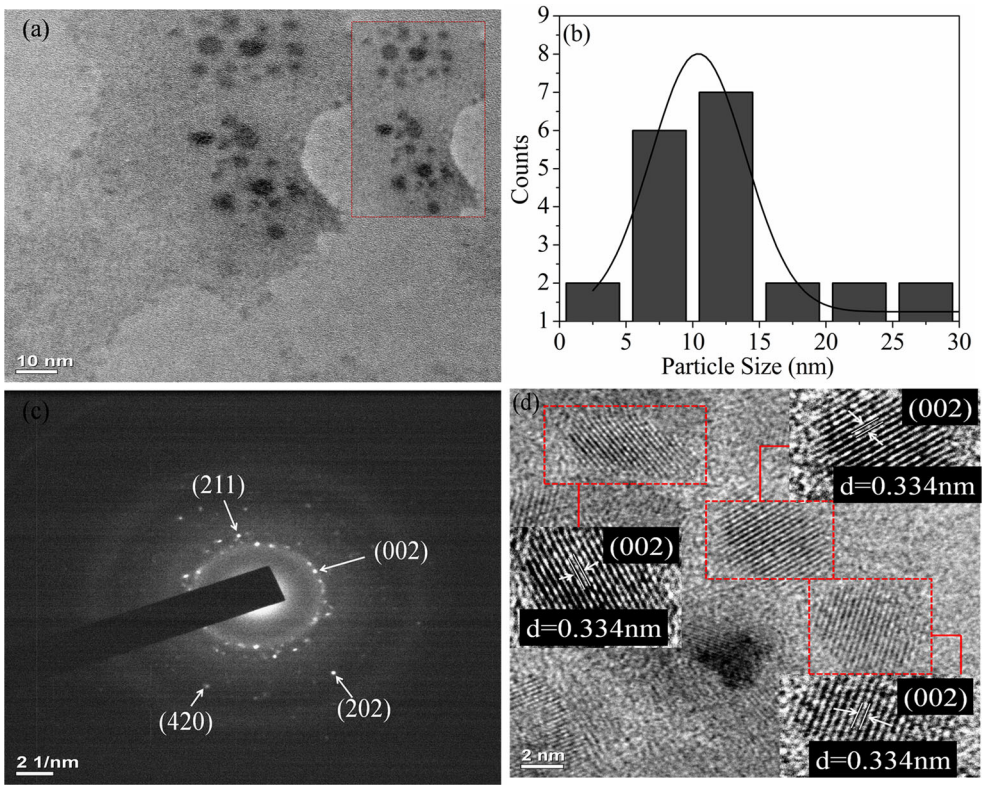

Figure 9. (**a**) TEM image (inset: magnified area), (**b**) corresponding particle size distribution histogram, (**c**) SAED pattern and (**d**) HRTEM image for sample S_3.

corroborated by the XRD results. The grain size in SEM images is greater than those of calculated from XRD as SEM shows an aggregate image of composed small grains or crystals [73].

Quantitative analysis of the $Cd_xPb_{1-x}S$ thin films is carried out using EDX spectroscopy to study the stoichiometry of the films. The EDX analysis confirms the presence of Cd, Pb and S in all the prepared films along with Si, C and O. Figure 8 shows the EDX spectra of $Cd_xPb_{1-x}S$ thin films for all samples S_1, S_2, S_3 and S_4, respectively, along with the atomic% ratio S/(Cd+Pb) of the films listed at the upper right corner of the respective EDX images. The presence of carbon is due to the carbon adhesive tape used to mount the samples. The presence of oxygen in the prepared $Cd_xPb_{1-x}S$ thin film samples can be attributed to the glass substrates where the thin films are fabricated and also, due to the deionized water solution from which the samples are synthesized. Si is attributed to only glass substrates. It is observed that the element Pb shows a decreasing trend, whereas Cd content shows an increasing trend in the samples. Similar results have been reported for PbS thin films with Ni doping by Rajashree and Balu [74]. This confirms that there is more Cd in the overall sample as expected, since Cd:Pb ratio in the films was higher. The atomic% ratio of S/(Cd+Pb) for samples S_1, S_2, S_3 and S_4 are 0.83, 0.86, 0.95 and 0.98, respectively. The results show that all the films show a consistent stoichiometry as atomic% ratio of S/(Cd+Pb) increases from 0.83 to 0.98 and approaches to stoichiometric ratio 1 with the increasing Cd in the deposited films.

3.6 *TEM, HRTEM and SAED pattern analysis of $Cd_xPb_{1-x}S$ thin films*

TEM and HRTEM image analyses are carried out to investigate the size of the particle and crystallographic orientation of the prepared thin film. TEM image and the corresponding particle size distribution histogram of sample S_3 are shown in figure 9a and b, respectively. The average size among 24 particles is $\sim$13 nm. The result is in good agreement with the result obtained from XRD method for sample S_3. Figure 9c shows the bright field image of the sample S_3 corresponding to SAED pattern and the SAED pattern reveals the polycrystalline nature of the film. The lattice planes (002) and (202) are corresponding to hexagonal CdS phase (JCPDS: 41-1049), the lattice plane (211) is corresponding to tetragonal PbS phase (JCPDS: 20-0596), and the plane (420) is corresponding to cubic PbS phase (JCPDS: 05-0592). Highly ordered and parallel lattices are observed in respective HRTEM images, which are shown in figure 9d. This suggests that the film's crystallization with lattice spacing $\sim$0.334 nm, which is associated with (002) lattice plane of hexagonal CdS phase (JCPDS: 80-0006). This result is confirmed by XRD and SAED pattern analyses. For sample S_3, the interplanar spacing along with crystal planes observed in HRTEM and SAED pattern are listed in table 4.

3.7 *Estimation of optical band gap energy*

The transmission spectra of the $Cd_xPb_{1-x}S$ thin films at different solute ratios of Pb:Cd is shown in figure 10 and the inset shows photographs of samples S_1, S_2, S_3 and S_4. All the films have good transmittance in the visible light range with an average transmittance of >70%, indicating good optical quality of the deposited films with low scattering or absorption losses. When Cd content increases in $Cd_xPb_{1-x}S$, the films become more transparent in wavelength >500 nm. The blue shift of the absorption edges is observed as compared to the band gaps of bulk CdS $\sim$2.4 eV [12] and bulk PbS $\sim$0.41 eV [5].

From the transmission data, the absorption coefficient α is calculated by equation (4) [75]:

$$\alpha = -\frac{1}{t}\ln(T), \tag{4}$$

where t is the thickness and was estimated by Tolansky method using equation (5) [76]:

$$t = \left(\frac{\Delta L}{L}\right)\lambda/2, \tag{5}$$

where L is the fringe width or spacing and $\Delta L/L$ the fractional discontinuity of the fringe system. The calculated values are listed in table 5. The film thickness decreases with the increase in Cd content due to the varying rates of Cd^{2+} ions generation with different Cd additions in $Cd_xPb_{1-x}S$ thin films, which affects the growth rate of the films [77]. In addition, the difference in solubility values between $Cd(OH)_2$ and $Pb(OH)_2$, also affects the film thickness [78].

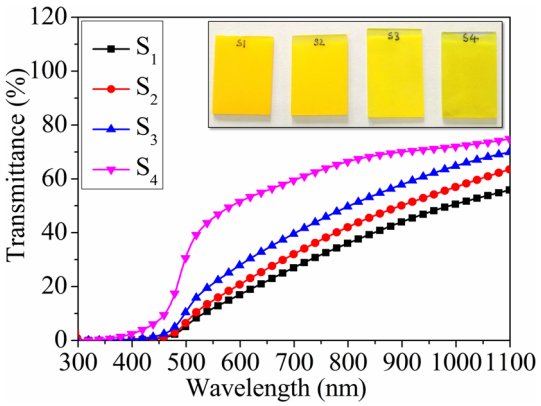

Figure 10. Plot of transmittance *vs.* wavelength of $Cd_xPb_{1-x}S$ thin film samples prepared at different solute ratios of (Pb:Cd): S_1 (3:7), S_2 (3:12), S_3 (3:17) and S_4 (3:22), respectively. Inset shows the photograph of prepared thin film samples S_1, S_2, S_3 and S_4.

Table 4. Structural parameters of $Cd_xPb_{1-x}S$ thin films estimated from TEM, HRTEM images and SAED pattern.

Sample code	Solute ratio	Average particle size (nm)	Interplanar spacing, *d* (nm)	*(hkl)* planes	Phase assignment
S_3	3:17	~13	0.334	(002)	Hexagonal-CdS
			0.256	(211)	Tetragonal-PbS
			0.157	(202)	Hexagonal-CdS
			0.131	(420)	Cubic-PbS

Table 5. Estimated thickness and optical band gap of $Cd_xPb_{1-x}S$ thin films.

Sample code	Thickness, *t* (nm)	Band gap energy, E_g (eV)
S_1	207	2.8
S_2	198	2.82
S_3	187	3
S_4	174	3.42

The optical band gap (E_g) value of the $Cd_xPb_{1-x}S$ films is estimated by equation (6) [75]:

$$\alpha h\nu = A\left(h\nu - E_g\right)^m \tag{6}$$

where A is the Tauc's slope, $h\nu$ the photon energy and m the transition probability. CdPbS semiconducting thin films show the direct band gap nature [1,66–68]. For direct band gap semiconductor, $m = 1/2$. Therefore, the $(\alpha h\nu)^2$ *vs.* $h\nu$ plots for samples S_1, S_2, S_3 and S_4, are shown in figure 11a. The calculated values of band gap are estimated in table 5. The optical band gap values for samples S_1, S_2, S_3 and S_4 are ~2.8, 2.82, 3 and 3.42 eV, respectively. Alloying of bulk PbS (E_g ~ 0.41 eV) with bulk CdS (E_g ~ 2.46 eV) is expected to vary the optical band gaps between 0.41 and 2.46 eV. The values of band gap increase with the increase in Cd content in $Cd_xPb_{1-x}S$ thin films and which are greater than the value of bulk CdS and PbS. This can be explained with Burstein–Moss effect [79]. In this effect, the Fermi level and its position depend on the concentration of the free electrons present in the conduction band [80]. In n-type $Cd_xPb_{1-x}S$ semiconductor, according to Burstein–Moss effect, the proximity of the conduction band will form additional carrier electrons leaving the Fermi level of PbS in the conduction band. The transition process will occur above the Fermi level rather than in the bottom of the conduction band because the gap between the bottom of conduction band and Fermi level will be filled with electrons [81]. Therefore, the energy band gap is associated with the excitation of the electrons from the valence band to Fermi level. The Fermi level which lies on the conduction band causes the absorption side to increase in energy and hence, results in widening of the band gap energy. Zhao and Li [81] synthesized Eu-doped PbS quantum dots and confirmed that band gap of Eu-doped PbS is bigger than both EuS and PbS. Yilmaz *et al* [82] synthesized Al-doped ZnO thin films and observed band gap values were greater than pure ZnO. These changes are similar to that observed in $Cd_xPb_{1-x}S$ thin films. The variation in the optical band gap as a function of Pb:Cd ratios is shown in figure 11b. The large modification in E_g confirms the formation of ternary $Cd_xPb_{1-x}S$ thin films [83]. So, it is concluded that by changing the Cd content in $Cd_xPb_{1-x}S$ films, the band

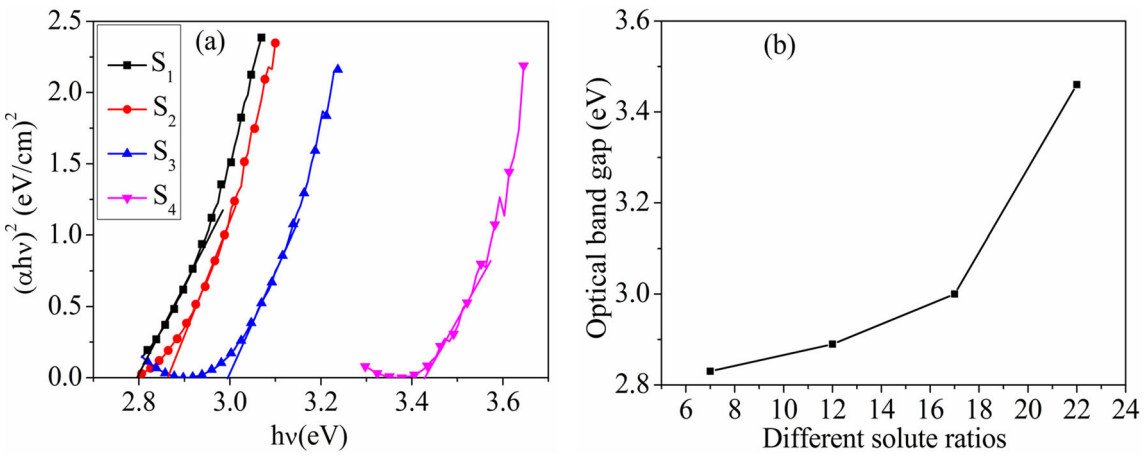

Figure 11. (**a**) Plots of $(\alpha h\nu)^2$ *vs.* $h\nu$. (**b**) Variation in band gap energy (E_g) as a function of different solute ratios of (Pb:Cd) for $Cd_xPb_{1-x}S$ thin film samples S_1, S_2, S_3 and S_4, respectively.

gap as well as transmittance of the films can be enhanced. Due to this property, the nanocrystalline $Cd_xPb_{1-x}S$ films are suitable for photovoltaic cells as a window layer.

4. Conclusions

Nanocrystalline $Cd_xPb_{1-x}S$ thin films are fabricated on glass substrates by CBD method as a function of different Pb:Cd ratios. The XRD studies indicate the mixture of cubic, hexagonal and tetragonal phase structures of $Cd_xPb_{1-x}S$ thin films. The line broadening was analysed by Scherrer's formula, W–H analysis and SSP method. From the result, it is observed that lattice strain increases and crystallite size decreases with increasing Cd content in $Cd_xPb_{1-x}S$ thin films. The film crystallinity is relatively good when the Cd content is low and deteriorates its crystallinity with increase in Cd content as confirmed by XRD spectra. Existence of different peaks of CdS and PbS nanoparticles in FTIR revealed the formation of $Cd_xPb_{1-x}S$ and the presence of different functional groups in the films. Micro-Raman spectra show the phase transition in all the prepared $Cd_xPb_{1-x}S$ thin films, due to variation in the Cd content in the films, where modes of cubic and hexagonal phases were observed. An increase in FWHM of cubic 1LO or hexagonal $A_1(LO)/E_1(LO)$ peak with increase in Cd content in the films is observed, which implies an increase in lattice damage. SEM image analysis confirms that all the films have uniform surface morphology with layered type structure. EDX confirms the presence of Cd, Pb, S in the prepared $Cd_xPb_{1-x}S$ films. The TEM image analysis shows an average particle size of $\sim$13 nm. The TEM result was in good agreement with the result of XRD method. HRTEM and SAED analyses reveal that $Cd_xPb_{1-x}S$ thin film exhibits polycrystalline nature with co-existence of hexagonal CdS, tetragonal and cubic PbS phases. The optical band gap energy values increase with the increase in the Cd content in the $Cd_xPb_{1-x}S$ films. The band gap energy values are greater than that of bulk value of both CdS and PbS.

Acknowledgements

We acknowledge the Department of Physics, Bahona College, Jorhat (India), for providing laboratory facilities. We acknowledge the CSIC, Dibrugarh University, Dibrugarh (India), for providing the SEM and EDX facilities. We acknowledge SAIF, Gauhati University, Guwahati (India), for providing PXRD facilities. We also acknowledge SAIF-NEHU, Shillong, Meghalaya (India), for TEM, HRTEM and SAED facilities. We acknowledge SAIC, Tezpur University, (India), for providing FTIR and micro-Raman facilities.

References

[1] Nair S B, Abraham A, Pradeep B, Shripathi T, Ganesan V and Philip R R 2014 *AIP Conf. Proc.* **1620** 511
[2] Tan G L, Liu L and Wu W 2014 *AIP Adv.* **4** 067107
[3] Deo S R, Singh A K, Desmukh L, Paliwai L J and Singh R S 2015 *Optik* **126** 2311
[4] Barote M A, Yadav A A and Masumdar E U 2011 *Chalcogenide Lett.* **8** 129
[5] Paulraj K, Ramaswamy S, Shkir M, Yahia J S, Hamdy M S and Al Faify S 2020 *J. Mater. Sci.: Mater. Electron.* **31** 1817
[6] Forostyanaya N A, Maskaeva L N, Smirnova Z I, Santra S, Zyryanov G V, Markov V F *et al* 2018 *Thin Solid Films* **657** 101
[7] Rajathi S, Kirubavathi K and Selvaraju K 2017 *J. Taibah Univ. Medical Sci.* **11** 1296
[8] Yıldırım A K and Altıokka B 2020 *Emerg. Mater. Res.* **9** 1
[9] Fouda A N, Marzook M, Abd EI-Khalek H M, Ahmed S, Eid E A and EI Basaty A B 2017 *Silicon* **9** 809
[10] Hone F G and Dejene F B 2020 *Inorg. Chem. Commun.* **111** 107583
[11] Ali S M, Al Garawi M S, Al Dawood S, Al Salman S A and Al Gamdi S S 2020 *Radiat. Phys. Chem.* **171** 108732
[12] Isik M, Gullu H H, Delice S, Parlak M and Gasanly N M 2019 *Mater. Sci. Semicond. Process.* **93** 148
[13] Laukaitis G, Lindroos S, Tamulevicius S, Leskela M and Rackaitis M 2000 *Appl. Surf. Sci.* **161** 396
[14] Ma L, Ali X and Wu X 2016 *J. Alloys Compd.* **691** 399
[15] Ahmad F R, Yakimov A, Davis R J, Her J H, Cournoyer J R and Ayensu N M 2013 *Thin Solid Films* **535** 166
[16] Mathew J and Anila E I 2018 *Sol. Energy* **172** 165
[17] Sinha T, Lilhare D and Khare A 2019 *J. Mater. Sci.* **54** 12189
[18] Arora L, Singh V N, Gupta P, Chhikara N, Jain K and Chand S 2014 *J. Nanosci. Nanotechnol.* **14** 5324
[19] Vaganova I V, Maskaeva L N, Markov V F, Voronin V I and Bamburov V G 2018 *Nanosyst.: Phys. Chem. Math.* **9** 811
[20] Nicholos P L, Liu Z, Yin L, Turkdogan S, Fan F and Ning C Z 2015 *Nano Lett.* **15** 909
[21] Gode F and Unlu S 2019 *Mater. Sci. Semicond. Process.* **90** 92
[22] Ahire R R and Sharma R P 2006 *Indian J. Eng. Mater. Sci.* **13** 140
[23] Agawane G L, Shin S W, Suryawanshi M P, Gurav K V, Moholkar A V, Lee J Y *et al* 2013 *Mater. Lett.* **106** 186
[24] Anuar K, Tan W T, Atan S, Kuang Z, Haron M J, Ho S M *et al* 2010 *Chem. Asian J.* **22** 222
[25] Ahmed H H, Khazeal A S and Atallah F S 2013 *J. Univ. Anbar Pure Sci.* **7** 1
[26] Bicer M and Sisman I 2011 *Appl. Surf. Sci.* **257** 2944
[27] Mahalingam T, Kathalingam A, Lee S, Moon S and Kim Y D 2007 *J. New Mater. Sci.* **10** 15
[28] Xiao F, Yoo B Y, Ryan M A, Lee K H and Myung N V 2006 *Electrochim. Acta* **52** 1101
[29] Ngo T T, Chavhan S, Kosta I, Miguel O, Grande H J and Ramon T Z 2014 *ACS Appl. Mater. Interfaces* **6** 2836
[30] Takashiri M, Tanaka S, Miyazaki K and Tsukamoto H 2007 *J. Appl. Phys.* **101** 074301
[31] Heras C and Sanchez C 1991 *Thin Solid Films* **199** 259

[32] Dizaji H R, Ghasemian M and Ehsani M H 2012 *Surf. Rev. Lett.* **19** 1250012

[33] Dedova T, Krunks M, Volobujeva O and Oja I 2005 *Phys. Status Solidi C* **5** 1161

[34] Isac L A, Duta A, Kriza A, Enesca I A and Nanu M 2007 *J. Phys. Conf.* **61** 477

[35] Sankapal B R, Mane R S and Lokhande C D 2000 *Mater. Res. Bull.* **35** 2027

[36] Guzeldir B, Saglam M and Ates A 2012 *Acta Phys. Pol. A* **121** 33

[37] Willeke G, Dasbach R, Sailer B and Bucher E 1992 *Thin Solid Films* **213** 271

[38] Hwang D H, Ahn J H, Hui K N, Hui K S and Son Y G 2012 *Nano. Res. Lett.* **7** 1

[39] Yao H, Shen H, Zhu X, Jiao J, Li J and Wang W 2016 *Ceram. Int.* **42** 2466

[40] Gogoi L, Chaliha S and Saikia P K 2018 *AIP Conf. Proc.* **1942** 140020

[41] Thangavel S, Ganesan S and Saravanan K 2012 *Thin Solid Films* **520** 5206

[42] Portillo-Moreno O, Lima-Lima H, Ramirez-Falcon V, Martinez-Juarez J, Juarez-Diaz G, Lozada-Morales R *et al* 2006 *J. Electrochem. Soc.* **153** 926

[43] Portillo M C, Moreno O P, Parez R G, Merino R P, Juarez H S, Tehuacanero Cuapa S *et al* 2017 *Mater. Sci. Semicond. Process.* **72** 22

[44] Yadav H K, Sreenivas K, Katiyar R S and Gupta V 2007 *J. Phys. D: Appl. Phys.* **40** 6005

[45] Badera N, Godbole B, Srivastava S B, Vishwarkarma P N, Sharath Chandra L S, Jain D *et al* 2008 *Appl. Surf. Sci.* **254** 7042

[46] Tsai C S, Chen S H and Chuu D S 1996 *Phys. Rev. B* **54** 11555

[47] Maskaeva L N, Markov V F and Guev A I 2003 *Dokl. Phys. Chem.* **390** 147

[48] Bhushan S, Mukherjee M and Bose P 2002 *J. Mater. Sci.: Mater. Electron.* **13** 581

[49] Kim D H, Lee D J, Kim N M, Lee S J, Kang T W, Woo Y D *et al* 2007 *J. Appl. Phys.* **101** 094111

[50] Prathap P, Revathi N, Venkata Subbaiash Y P and Reddy K T R 2008 *J. Phys.: Condens. Matter* **20** 035205

[51] Palomino Merino R, Portillo Moreno O, Chaltel Lima L A, Gutiérrez Pérez R, De Icaza Herrera M and Castaño V 2013 *J. Nanomater.* **507647** 1

[52] Kittel C 2004 *Introduction to solid state physics* 8th edn (Wiley) p 25

[53] Zak A K, Majid W H A, Abrishami M E and Yousefi R 2011 *Solid State Sci.* **13** 251

[54] Borah D J and Mostako A T 2020 *Appl. Phys. A* **126:818** 1

[55] Tagliente M A and Massaro M 2008 *Nucl. Instrum. Meth. Phys. Res. B* **266** 1055

[56] Mote V D, Purushotham Y and Dole B N 2012 *J. Theor. Appl. Phys.* **6** 6

[57] Pawar S B, Shaikh J S, Devan R S, Ma Y R, Haranath D, Bhosale P N *et al* 2011 *Appl. Surf. Sci.* **258** 1869

[58] Aziz B S, Rasheed M A, Saeed S R and Abdullah O G 2017 *Int. J. Electrochem. Sci.* **12** 3263

[59] Heiba Z K, Mohamed M B, Abdellatief M and Albassam A A 2020 *Appl. Phys. A* **126:518** 1

[60] Sharma S, Reddy A V D, Jayarambabu N, Kumar N V M, Saineetha A, Kailsa S *et al* 2020 *Mater. Today Proc.* **26** 162

[61] Ranjan R and Sinha A S K 2019 *Int. J. Hydrog. Energy* **44** 5955

[62] Poornaprakash B, Chalapathi U, Kumar M, Subramanyam K, Vattikuti S V P, Reddy M S P *et al* 2020 *Ceram. Int.* **46** 21728

[63] Sabah A, Siddiqui S A and Ali S 2010 *World Acad. Sci. Eng. Technol.* **69** 82

[64] Gahramanli L, Muradov M, Kukovecz A, Balayeva O and Eyvazova G 2020 *Inorg. Nano Met. Chem.* **50** 1

[65] Zahn D R T, Maierhofer Ch, Winter A, Reckzugel M, Sarma R, Thomas A *et al* 1991 *J. Vac. Sci. Technol. B* **9** 2206

[66] Khallaf H, Chai G, Lopan O, Chow L, Park S and Schulte A 2008 *J. Phys. D: Appl. Phys.* **41** 185304

[67] Lee J 2004 *Thin Solid Films* **451–452** 170

[68] Arguello C A, Rousseau D L and Porto S P S 1969 *Phys. Rev.* **181** 1351

[69] Tell B, Damen T C and Porto S P S 1966 *Phys. Rev.* **144** 771

[70] Nusimovici M A and Birman J L 1967 *Phys. Rev.* **156** 925

[71] Enderlein T R and Leite J R 1996 *J. Appl. Phys.* **79** 4137

[72] Najmaei S, Liu Z, Ajayan P M and Lou L 2012 *Appl. Phys. Lett.* **100** 013106

[73] Munaga V V P, Krishnan T and Borra R K 2020 *SN Appl. Sci.* **2:552** 1

[74] Rajashree C and Balu A R 2016 *Optik* **127** 8892

[75] Borah D J, Mostako A T T, Saikia P K and Dutta P 2019 *Mater. Sci. Semicond. Process.* **93** 111

[76] Tolansky S 1970 *Phys. Today* **23** 95

[77] Kapriper A, Guneri E, Code F, Gamus C and Ozpozan T 2011 *Mater. Chem. Phys.* **129** 183

[78] Mahdi M A and Al-Ani S K J 2012 *Int. J. Nanoelectron. Mater.* **5** 11

[79] Yogamalar N R and Bose A C 2011 *Appl. Phys. A* **103** 33

[80] Kaur M, Kaur P, Kaur G, Dev K, Negi P and Sharma R 2018 *Vacuum* **155** 689

[81] Zhao Y and Li W 2019 *Mater. Res. Express* **6** 115908

[82] Yilmaz M, Tatar D, Sonmez E, Cirak C, Aydogan S and Gunturku R 2015 *Synth. React. Inorg. Met. Org. Chem.* **46** 489

[83] Thangavel S, Ganesan S, Chandramohan S, Sudhagar P, Kang Y S and Hong C H 2010 *J. Alloys Compd.* **495** 234